The Annual Cycle of the Energy Budget. Part I: Global Mean and Land–Ocean Exchanges

JOHN T. FASULLO AND KEVIN E. TRENBERTH

National Center for Atmospheric Research, Boulder, Colorado*

(Manuscript received 7 March, in final form 1 October 2007)

ABSTRACT

The mean and annual cycle of energy flowing into the climate system and its storage, release, and transport in the atmosphere, ocean, and land surface are estimated with recent observations. An emphasis is placed on establishing internally consistent quantitative estimates with discussion and assessment of uncertainty. At the top of the atmosphere (TOA), adjusted radiances from the Earth Radiation Budget Experiment (ERBE) and Clouds and the Earth's Radiant Energy System (CERES) are used, while in the atmosphere the National Centers for Environmental Prediction–National Center for Atmospheric Research (NCEP–NCAR) reanalysis and 40-yr European Centre for Medium-Range Weather Forecasts (ECMWF) Re-Analysis (ERA-40) estimates are used. The net upward surface flux (F_S) over ocean is derived as the residual of the TOA and atmospheric energy budgets, and is compared with direct calculations of ocean heat content (O_E) and its tendency ($\delta O_E/\delta t$) from several ocean temperature datasets. Over land, F_S from a stand-alone simulation of the Community Land Model forced by observed fields is used. A depiction of the full energy budget based on ERBE fluxes from 1985 to 1989 and CERES fluxes from 2000 to 2004 is constructed that matches estimates of the global, global ocean, and global land imbalances. In addition, the annual cycle of the energy budget during both periods is examined and compared with ocean heat content changes.

The near balance between the net TOA radiation (R_T) and F_S over ocean and thus with O_E, and between R_T and atmospheric total energy divergence over land, are documented both in the mean and for the annual cycle. However, there is an annual mean transport of energy by the atmosphere from ocean to land regions of 2.2 ± 0.1 PW (1 PW = 10^{15} W) primarily in the northern winter when the transport exceeds 5 PW. The global albedo is dominated by a semiannual cycle over the oceans, but combines with the large annual cycle in solar insolation to produce a peak in absorbed solar and net radiation in February, somewhat after the perihelion, and with the net radiation 4.3 PW higher than the annual mean, as it is enhanced by the annual cycle of outgoing longwave radiation that is dominated by land regions. In situ estimates of the annual variation of O_E are found to be unrealistically large. Challenges in diagnosing the interannual variability in the energy budget and its relationship to climate change are identified in the context of the episodic and inconsistent nature of the observations.

1. Introduction

The primary driver of Earth's climate system is the uneven distribution of net downward radiation (R_T) at the top of the atmosphere (TOA; see appendix A for a list of acronyms and variables used in this paper) owing principally to sun–Earth geometry. Upon entering the system, the incoming radiative flux is partitioned among internal heat, and potential, latent, and kinetic energy (Trenberth and Stepaniak 2004). While basic aspects of the global mean TOA budget, such as the near balance between absorbed solar radiation (ASR) and outgoing longwave radiation (OLR), have long been known (Dines 1917), the quantification of the flow and storage of energy, and the conversions among different forms of energy, has evolved continually. Moreover, the full energy budget, which is composed of multiple flux, transport, and storage terms, has been assessed only rarely.

Kiehl and Trenberth (1997) provided an assessment of the global annual mean budget at the TOA and for

* The National Center for Atmospheric Research is sponsored by the National Science Foundation.

Corresponding author address: Kevin Trenberth, NCAR, P.O. Box 3000, Boulder, CO 80307-3000.
E-mail: trenbert@ucar.edu

DOI: 10.1175/2007JCLI1935.1

the atmosphere based on a mix of observations and model results. Major recent advances in understanding the energy budget have been provided by satellite data and globally gridded reanalyses (e.g., Trenberth et al. 2001; Trenberth and Stepaniak 2003a,b). Trenberth et al. (2001) performed comprehensive estimates of the atmospheric energy budget based on two first-generation atmospheric reanalyses and several surface flux estimates, and made crude estimates of uncertainty. Trenberth and Caron (2001) inferred the net surface fluxes as a residual of TOA satellite measurements and the atmospheric energy budget, and computed meridional ocean heat transports as a residual. Although physical constraints on the requirement for a global mean energy balance adjusted for effects of climate change were used, no error analysis of the satellite data was included. However, inferred annual mean meridional energy transports in the ocean agreed with direct estimates to within error bars of order 0.3 PW (1 PW = 10^{15} W; Trenberth and Caron 2001). The atmospheric energy budget has been documented in some detail for the annual cycle (Trenberth and Stepaniak 2003a, 2004) and for El Niño–Southern Oscillation (ENSO) and interannual variability (Trenberth et al. 2002; Trenberth and Stepaniak 2003a). Challenges remain, however, and in this paper new observations, improved estimates of the current TOA and surface imbalances, and a more holistic approach allow for improvements in the budget to be made and for uncertainty estimates to be constructed. Also addressed here is the quantification of the mean annual cycle and land–ocean exchanges, including a decomposition of the energy flows for the ocean and land domains, as this allows the constraints of the two systems to be exploited. Moreover, a comparison of the residuals from the TOA and atmospheric budgets at the surface with independent measurements of integrated ocean heat content is presented, and thus surface fluxes are better quantified.

A schematic of the flows of energy and the notation used are given in Fig. 1. At the TOA, the dominant energy terms include solar insulation (SI), ASR, and OLR, with R_T = ASR − OLR. Upon entering the climate system, energy imbalances at the TOA can be partitioned mainly between the divergence and the tendency of total atmospheric energy (A_E) and oceanic energy (O_E), including sea ice, and secondarily by changes in land energy storage (L_E), and energy transport by rivers. In the atmosphere, the transport of energy ($\mathbf{F}_A$) and its divergence, $\nabla \cdot \mathbf{F}_A$, dominate the tendency locally. Although the atmosphere represents only a fraction of the climate system's heat capacity [equivalent to 3.5 m of ocean; Trenberth and Stepaniak (2004)], it is the dominant contributor to the mean poleward transport of energy outside of the tropics (Trenberth and Caron 2001). While globally over long time scales R_T is small, its annual cycle is considerable owing principally to fluctuations in Earth's albedo and SI, as Earth orbits through its perihelion (3 January) and aphelion (3 July). The associated annual cycle of the global mean R_T is on the order of 20 W m^{-2} from peak to trough or, integrated globally, about 10 PW (e.g., Kyle et al. 1993). This is large compared with the estimated total TOA imbalance arising from the changing atmospheric composition, which Hansen et al. (2005) estimated recently at 0.85 ± 0.15 W m^{-2}. On monthly time scales, the regional variability of the total atmospheric energy tendency ($\delta A_E/\delta t$) and the divergent energy flux ($\nabla \cdot \mathbf{F}_A$) associated with R_T are considerable (Trenberth and Stepaniak 2003a). Stationary and transient components of atmospheric dry static, latent, and kinetic energy transports combine and, in instances, mutually compensate to result in a seamless poleward transport of energy that belies the complexity of the

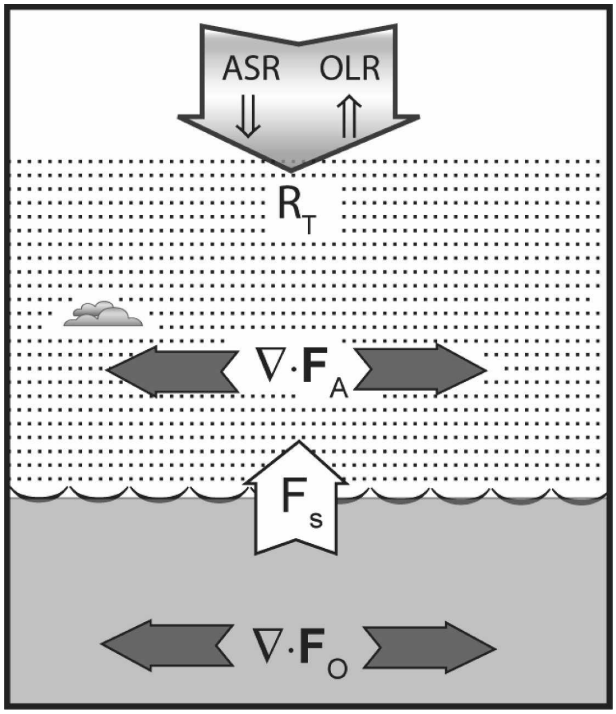

FIG. 1. Schematic of the energy balance illustrating the notation and direction of the fluxes. The ASR is directed down, OLR is upward, and their net R_T is downward, while the surface flux F_s is upward. The net fluxes into the atmosphere and ocean are mostly balanced by the atmospheric and oceanic divergences of the energy transports $\mathbf{F}_A$ and $\mathbf{F}_O$ (as shown), and the changes in energy storage (not shown). For land, there is no internal transport of consequence and the surface flux is balanced by the storage changes.

physical mechanisms of which it is composed (Trenberth and Stepaniak 2003a,b). The TOA and atmospheric budgets are closed by the net upward surface energy flux (F_S), which consists principally of shortwave and longwave radiative fluxes and turbulent fluxes of latent and sensible heat. In the ocean, F_S in the tropics is balanced principally by the transport of ocean energy (mainly heat) ($\mathbf{F}_O$) and its divergence ($\nabla \cdot \mathbf{F}_O$), while in midlatitudes it is largely balanced locally by changes in ocean heat storage $\delta O_E/\delta t$ (Jayne and Marotzke 2001; Trenberth et al. 2001).

Estimation of F_S is particularly challenging, as in situ estimates contain considerable systematic and random uncertainties that frequently exceed 25 W m^{-2} (Gleckler and Weare 1997; Yu et al. 1999). If even a small component of the uncertainty (e.g., 10% or 2.5 W m^{-2}) is systematic, the associated global budget uncertainty (1.3 PW) can obscure key characteristics of the TOA and surface budgets. Estimates of F_S from reanalyses are model derived and contain errors (Trenberth et al. 2001, 2002). Perhaps most troublesome is that the errors are both random and systematic, and the data thus fail to satisfy basic global constraints.

An alternative is based on deriving F_S over ocean from the residual of the TOA and reanalysis atmospheric budgets (Trenberth 1997). While the regional error of this method is of similar magnitude to that of in situ estimates, the error converges to be the largely random error in the TOA estimates because the systematic TOA bias is first removed, the global mean $\nabla \cdot \mathbf{F}_A$ is zero by construction, and $\delta A_E/\delta t$ is small generally. With climate change, a small imbalance in F_S exists and there is an order of 0.5 PW net TOA heat flux (Hansen et al. 2005), which can be further separated into its land [<0.1 PW; Huang (2006)] and ocean [~0.4 PW; Willis et al. (2004)] components. These present-day estimates compare favorably in relative importance to those of Levitus et al. (2005), who estimated the contributions of the imbalance from 1955 to 1998 to the oceans (0.10 PW) and continental landmasses and glaciers (0.01 PW). An open science question addressed here is whether the atmospheric reanalyses, in conjunction with available estimates of R_T, are able to attain accuracy in $\nabla \cdot \mathbf{F}_A$, and thus in F_S, that are suitable for resolving simultaneously the global, global ocean, and global land annual cycles and net imbalances from this residual method.

The purposes of the present manuscript are therefore 1) to explore the current range of observations of the global, global land, and global ocean energy budgets and their annual cycles; 2) to develop estimates of uncertainty for each term; and 3) to establish a comprehensive best estimate of the present-day budget. The term best is used in the sense of "best practice"[1] in recognition of the fact that successive data and analyses are likely to improve upon the results presented here. Section 2 describes the data and methods while section 3 documents aspects of the mean energy cycle, both for the globe and for global land and global ocean domains. The results are presented in section 4, followed by discussion (section 5), and then concluding remarks (section 6). This paper deals with the global, land, and ocean domain averages, but it is essential to delve into the full spatial structure to determine uncertainties and sources of error. The meridional structure and poleward transports are therefore documented in Fasullo and Trenberth (2008) and the full three-dimensional aspects for the ocean are presented in Trenberth and Fasullo (2008), where a more complete error analysis is performed.

2. Data and methods

In dealing with energy and its partitioning, we have found that it is important to ensure conservation by dealing with actual amounts, generally expressed in terms of petawatts rather than watts per square meter. Moreover, in communicating the relative importance of the various energy terms—as a function of latitude for example—PW is the preferred unit as this integrated quantity is more directly relevant to 1) understanding the balances and closures that exist in the budget and 2) portraying realistically the relative magnitude of the multiple energy terms. In instances, area-average quantities are used for reference to earlier works. The conversion globally is 1 W m^{-2} = 0.510 PW; over the global ocean, 1 W m^{-2} = 0.372 PW; and over the global land, 1 W m^{-2} = 0.138 PW.

a. Energy budgets

The atmospheric energy budget equation, when vertically integrated (Trenberth 1997), can be written as

$$\frac{\partial A_E}{\partial t} + \nabla \cdot \mathbf{F}_A = \mathrm{ASR} - \mathrm{OLR} + F_s, \qquad (1)$$

where

$$\mathbf{F}_A = \frac{1}{g}\int_0^{p_s} \mathbf{v}(c_p T + \Phi + k + Lq)\,dp \quad \text{and}$$

$$A_E = \frac{1}{g}\int_0^{p_s} (c_p T + \Phi_s + k + Lq)\,dp.$$

[1] "Best practice" is a management idea that asserts a technique, method, or process is more effective at delivering a particular outcome than any other.

Here, $\mathbf{F}_A$ is the total vertically integrated atmospheric energy transport. The fields k, T, $\mathbf{v}$, q, p, and z denote the atmospheric kinetic energy, temperature, wind, specific humidity, pressure, and geopotential height, respectively, and $\Phi = gz$ is the geopotential. Standardized values a, g, c_p, and L correspond to Earth's radius, the acceleration due to gravity, the specific heat of air at constant pressure, and the latent heat of vaporization, respectively. The subscript s refers to the surface. Note that the atmospheric energy includes a surface geopotential term and the quantity in brackets differs from the total energy that is transported owing to the pressure–work term in the thermodynamic equation. Consequently, the terms in $\mathbf{F}_A$ consist of the transport of the sensible heat, potential energy, kinetic energy, and latent energy, and the first two can be combined as the dry static energy, which, when combined with the last term, Lq, give the moist static energy. We note that R_T = ASR − OLR and F_s have been previously defined. By definition the divergent term in (1) drops out for global mean budgets while for the full four-dimensional fields, both the meridional and zonal energy transports must be considered.

As previously discussed, F_S over ocean is diagnosed from the residual of the atmospheric budget such that

$$F_S = \partial A_E/\partial t + \nabla \cdot \mathbf{F}_A - R_T. \tag{2}$$

We introduce the notation that a superscript corresponds to the domain: g (global), l (land), and o (ocean). As the annual mean of F_S^l is approximately zero (e.g., Huang 2006), the net transport of energy from ocean to land can be estimated from

$$\overline{\mathbf{F}_A(\text{ocean} \rightarrow \text{land})} = \overline{R_T^l} + \overline{\frac{\partial A_E^l}{\partial t}}, \tag{3}$$

where the overbar corresponds to annual averaging. Additionally, the integrated O_E is computed to include only the heat content, as changes in oceanic kinetic energy and geopotential are small, such that

$$O_E = \int \rho T(z)\, C_w\, dz, \tag{4}$$

where z is the depth of the ocean, T is the ocean temperature, and ρ and C_w are the density specific heat of seawater, respectively. The ocean datasets used to diagnose T include the *World Ocean Atlas 2005* (*WOA*; Locarnini et al. 2006), the ocean analysis of the Japanese Meteorological Agency Version 6.2 (JMA; Ishii et al. 2006), and the recently corrected Global Ocean Data Assimilation System (GODAS; Behringer and Xue 2004; Behringer 2007).

An independent estimate of global ocean F_S can be obtained as a residual from

$$F_S^o = \partial A_E^g/\partial t - R_T^g - F_S^l, \tag{5}$$

and for the global ocean from

$$\partial O_E/\partial t = -F_S^o. \tag{6}$$

The challenges posed in diagnosing the terms in (1) include achieving adequate sampling of the sizable spatial and temporal gradients associated with radiative fluxes $\nabla \cdot \mathbf{F}_A$ and F_S, and diagnosing atmospheric fields accurately, particularly with regard to tropical moisture, geopotential height, and extratropical temperature, whose transports are the dominant contributors to the total energy divergence. Satellite measurements provide the "best estimate" of the TOA terms in (3) while the most comprehensive estimates of the global atmospheric temperature and moisture fields are available from the National Centers for Environmental Prediction–National Center for Atmospheric Research (NCEP–NCAR) reanalysis (NRA) and the second-generation 40-yr European Centre for Medium Range Weather Forecasts (ECMWF) Re-Analysis (ERA-40). Contemporaneous discrepancies between the reanalyses provide an important initial estimate of the uncertainty in the atmospheric energy storage and flow. The value of F_S^l averaged over long time periods is small, but its annual cycle, which is associated primarily with energy storage, is nonnegligible (Dai and Trenberth 2002). As direct observations of F_S^l are few, model simulations from the Community Land Model (CLM) forced by the observed fields are used (Qian et al. 2006), as described below.

b. Satellite retrievals

Satellite retrievals from the Earth Radiation Budget Experiment (ERBE; Barkstrom and Hall 1982) and the Clouds and the Earth's Radiant Energy System (CERES; Wielicki et al. 1996) datasets are used. ERBE estimates are based on observations from three satellites [*Earth Radiation Budget Satellite* (*ERBS*), and *National Oceanic and Atmospheric Administration* (*NOAA*)*-9* and *-10*] for February 1985–April 1989 and the details of the data and its adjustments are given in appendix B. While agreeing with available estimates of the global radiative imbalance, our ERBE-adjusted product also compensates for the discontinuity in the inferred ocean-to-land energy transport from (3) that results from the loss of *NOAA-9* and matches the OLR trend from 60°S to 60°N as reported by *ERBS* during the ERBE period.

The CERES instruments used here [Flight Model 1 (FM1) and FM2] are flown aboard the *Terra* satellite,

which has a morning equatorial crossing time and was launched in December 1999 with data extending to May 2004. We also make some use of CERES measurements onboard *Aqua* (from instruments FM3 and FM4), which had an afternoon equatorial crossing time, but the data are limited as it was launched in May 2002. CERES benefits from improved angular distribution models and scene identification relative to ERBE, owing in part to its enhanced scanner resolution and has achieved unprecedented instrument stability and calibration accuracy (Loeb et al. 2000, 2007). The CERES TOA Surface Radiation Budget (TOASRB) FM1 *Terra* Moderate Resolution Imaging Spectroradiometer (MODIS) Edition 2D Rev 1, product used here is reported on a 1° grid and is hereafter referred to as TOASRB. For more direct comparison to ERBE fluxes, CERES "ERBE-like" fields are also used and are based on upscaled radiances and ERBE algorithms applied to single satellite retrievals. In interpreting the differences between the ERBE and CERES fields, it is important to recognize the different time periods, retrieval methodologies, and retrieval instruments used. Among the methodological differences, the use of less accurate angular distribution models and crude cloud and surface scene identification in the ERBE retrieval process are fundamental (Ye and Coakley 1996). Key among structural differences is the coarser footprint and improved multisatellite sampling of the ERBE retrievals. Hence, it is not possible to isolate the natural variability from direct ERBE–CERES comparisons, even through the use of CERES ERBE-like products. Instances of missing data in the CERES datasets are treated in the same manner as for ERBE in Trenberth (1997) with a cosine fit to the annual cycle in albedo used to infer reflected solar radiation for regions of missing data. Typically, this accounts for most of the variance but it is undesirable to add a second harmonic as it raises the possibility that the albedo will exceed unity and become unphysical.

A comprehensive error analysis of the CERES mean budget (Wielicki et al. 2006), summarized in Table 1, addresses the difference between current estimates of the TOA imbalance (Hansen et al. 2005; Willis et al. 2004; Huang 2006) and the global mean imbalance of 6.4 W m^{-2} reported by TOASRB. While each error source is likely a very small percentage of the retrieved flux, the combined uncertainties can be significant. Indeed it is evident that if these errors stand up to further scrutiny, then they are not random but must all have the sign to enable them to add up to the observed physically unrealistic imbalance. Key among the error sources (>0.5 W m^{-2}) are total solar irradiance (TSI) and absolute calibration. Multiple secondary sources of error (<0.5 W m^{-2}) relate to sampling issues and assumptions of satellite altitude and near-terminator fluxes.

TABLE 1. Maximum likely contribution to the error in the CERES annual mean R_T estimates from several sources. These errors are taken from Wielicki et al. (2006) and must add constructively to reconcile R_T from CERES with independent best estimates of the global imbalance (e.g., Hansen et al. 2005; Huang, 2006). The terms are distinguished for shortwave (SW) and longwave (LW) components (W m^{-2}).

Error source	SW	LW	R_T
Total solar irradiance (1361 vs 1365 W m^{-2})	+1.0	0.0	+1.0
Absolute calibration	1.0	1.0	2.0
Spectral correction	0.5	0.3	0.8
Spatial sampling	<0.1	<0.1	<0.1
Angle sampling	+0.2	−0.1	+0.1
Time sampling (diurnal)	<0.2	<0.2	<0.2
Reference altitude (20 km)	0.1	0.2	0.3
Twilight SW flux (−0.25 W m^{-2})	<0.1	0.0	<0.1
Near terminator SW flux	+0.7	0.0	+0.7
3D cloud optical depth bias	+0.7	0.0	+0.7
Cumulative contribution			6.4

To achieve an estimate of TOA fluxes that matches current estimates of the global imbalances (Hansen et al. 2005; Willis et al. 2004; Huang 2006), we make a number of adjustments to the CERES TOASRB retrievals. An upper bound on the longwave adjustment per Table 1 is 1.5 W m^{-2} and, as the bulk of the uncertainty relates to absolute calibration, OLR is therefore increased uniformly by this amount in constructing a best estimate. To address the remaining error, we scale albedo rather than ASR directly, as per Trenberth (1997). The net imbalance in R_T is reduced to an acceptable, but imposed, 0.5 PW (about 1 W m^{-2}; a scaling of +0.303% for FM1 and +0.308% for FM2). As no explicit tuning is done in the CERES retrieval process itself, the adjustments made here are thus the only empirically derived corrections applied to the CERES fields. Future CERES products may well improve these estimates.

In addition to the uncertainties listed in Table 1, the estimation of the climatological mean fluxes from observations spanning a limited number of years is subject to errors associated with the interannual variability, which has been estimated at 0.25 PW (0.5 W m^{-2}) for the TOA fluxes (Ardanuy et al. 1992). Associated uncertainty estimates, equal to two sample standard deviations of interannual variability ($2\sigma_I$), are reported. Moreover, the impacts of diurnal aliasing, which have already been provided by Wielicki et al. (2006) for climatological fluxes (Table 1), have yet to be fully docu-

mented for annual cycle aspects of the energy budget. To quantify these impacts, mean fluxes from the ERBE-like *Terra* (FM1 + FM2) retrievals are contrasted with those of the *Aqua* (FM3 + FM4) satellite. Their difference is reported as Δ_D later (Tables 4–6). As differences in mean fluxes between the sensors relate primarily to satellite calibration, and thus preclude a meaningful evaluation of the impact of diurnal sampling on mean fluxes, only fields relating to variability across the annual cycle are evaluated for Δ_D, as for such calculations calibration biases are largely subtracted out by removing the annual mean.

c. Reanalysis datasets

While some previous studies (Yu et al. 1999) have relied on reanalysis fields that are purely model derived, here we use only fields strongly influenced by observations, such as surface pressure, winds, atmospheric temperature, and humidity (Kalnay et al. 1996). We use the NRA (Kistler et al. 2001) and the second-generation ERA-40 (Uppala et al. 2005). Trenberth et al. (2001) described how all of the energy terms for the atmosphere, their transports, and divergences are computed, and compared results for NRA and the first-generation 15-yr ECMWF Re-Analysis (ERA-15). These have now also been computed for ERA-40 and updated for NRA (all data are available online at http://www.cgd.ucar.edu/cas/catalog). Precipitation minus evaporation is computed from the atmospheric moisture budget rather than by differencing the model-derived fields of precipitation and evaporation (Trenberth and Guillemot 1998; Trenberth et al. 2001). Nonetheless, there are known problems with both NRA and ERA-40 (e.g., Trenberth et al. 2005; Uppala et al. 2005), and indeed it is a goal of the present study to further explore the limits of the reanalyses in assessing the energy budget.

d. Land model integrations

The seasonal variation of F_S^l is taken from a stand-alone integration of the CLM (Bonan et al. 2002; Qian et al. 2006). The CLM represents the surface with five primary subgrid land cover types, 16 plant functional types, and 10 layers for soil temperature and water, with explicit treatment of liquid water and ice. Representation of the seasonal cycle by the CLM shows significant improvements over previous-generation models (Bonan et al. 2002). In the stand-alone integration used here, the CLM is forced with observed fields infilled with high-frequency information from the NRA where observations are unavailable (Qian et al. 2006). The CLM reports fields on a T42 grid, with 128 longitude and 64 latitude points, on a monthly basis from 1948 through 2004.

e. Ocean surface fluxes and storage

The accuracy in calculating F_S^o using (2) is on the order of 20 W m^{-2} over 1000-km scales (Trenberth et al. 2001). The uncertainty in F_S is governed by the uncertainties in R_T, $\nabla \cdot \mathbf{F}_A$, and $\delta A_E/\delta t$, which on large scales are much less than those associated with the explicit modeling of surface radiative and turbulent fluxes. Because $\nabla \cdot \mathbf{F}_A$ is zero globally by definition, a cancellation of errors must occur over larger scales.

Estimates of ocean temperature are taken from three datasets: the *WOA*, JMA, and GODAS, which were current as of January 2007. The *WOA* fields are based on climatological monthly mean estimates of observed data after about 1960, the majority of which occur in the 1980s and 1990s. The estimates are thus not concurrent with either the ERBE or CERES periods, and reported differences with F_S must be considered in the context of σ_I, which can be estimated from the Japan Meteorological Agency (JMA) and Global Ocean Data Assimilation System (GODAS) fields. The JMA fields report monthly mean values from 1945 to 2005 and thus allow for the estimation of O_E and σ_I. In contrast to *WOA* and JMA, GODAS estimates are derived from the assimilated observed ocean temperature and salinity with estimates of surface forcing (wind stress, heat flux, and $E - P$) taken from NRA2, SST relaxed to the weekly NCEP analysis, and salinity relaxed to the *WOA* monthly climatology. The forcings are applied to the Modular Ocean Model, version 3 (MOM3), spanning 1980–2005.

To calculate O_E, $\delta O_E/\delta t$, and $\nabla \cdot \mathbf{F}_O$ in (2)–(4) from these data, the density and specific heat of ocean water are approximated as 1026.5 kg m^{-3} and 3990 J kg^{-1} K^{-1}, respectively. A recent *WOA* analysis (Antonov et al. 2004) of heat content assumes the density of seawater ρ is 1020 kg m^{-3} and the specific heat C_w is 4187 J kg^{-1} K^{-1}, whereas for the typical salinity of the ocean of ~35 psu, ρ is approximately 1028–1025 kg m^{-3}, and C_w is 3985–3995 J kg^{-1} K^{-1} for temperatures from 2° to 20°C. The product ρC_w is more nearly constant than either of the two components but the Antonov et al. (2004) value may be 4.4% too high, leading to an overestimate of the O_E and its annual cycle. We have performed our own integration using the 0-, 10-, 20-, 30-, 50-, 75-, 100-, 125-, 150-, 200-, and 250-m standard *WOA* levels. The depth of each layer is assumed to extend between the midpoints of the indicated depths. In the case of the surface, the layer is assumed to begin at 0 m, and at 250-m depth the layer is assumed to terminate at 275 m—half way to the next *WOA* layer at 300 m. The levels above

300 m reported by JMA are identical to those of *WOA* while the GODAS vertical resolution exceeds that of *WOA*, thus providing better resolution of the gradients with depth and the thermocline. In computing O_E, we further edit out the obvious spurious values south of 20°S by accepting only the monthly departures from the annual mean that are within two standard deviations of the zonal mean, and in this way we take advantage of the lack of land and presumed homogeneity over the southern oceans. Globally, the data are filtered temporally by retaining only the first three harmonics of the annual cycle. Oceanic heat tendencies are then computed by reassembling the Fourier series and differencing the heat content between the start and end of each month. As the GODAS fields are not global, but rather span 74°S–65°N, JMA estimates have been used to infill the GODAS fields in the polar regions. The contribution of variability in such filled regions to the global O_E is found to be largely insignificant, because of both the limited area and seasonal variability of such regions. Our O_E fields agree better with the Levitus and Antonov (1997) 12-month harmonic values than their total fields. Other small systematic differences may arise from the methods of compiling the vertical integral and numerical aspects in computing O_E [which are not described by Antonov et al. (2004)].

f. Secondary terms

In addition to the energy budget uncertainties, terms of secondary importance also exist, including the heat flux associated with river runoff and other water flows from land areas to ocean, and the latent heat flux associated with the seasonal sea ice variability. Scale analysis can be used to show the net contributions of these terms to be small, however, compared to $\nabla \cdot \mathbf{F}_A$ and F_S. For land, the net river runoff is approximately 4×10^4 km^3 yr^{-1} (Trenberth et al. 2007). If the 850-hPa–surface temperature difference (~10 K) is used to approximate the mean difference between the advected water vapor and river runoff, and a specific heat of 4218 J kg^{-1} is assumed, a net heat flux of 0.05 PW from land to ocean is estimated. For sea ice, estimates of Artic sea ice extent and volume (Koberle and Gerdes 2003) have a seasonal cycle of about 8×10^3 km^3. Assuming that ice has a density of 917 kg m^{-3} and heat of fusion of 3.35 kJ kg^{-1}, the peak heat flux associated with the seasonal cycle is ~0.5 PW. However, for the global ocean, the seasonal cycle in the Arctic is balanced by an approximately out-of-phase seasonal cycle in the Antarctic, for which reliable estimates of ice volume seasonality are not presently available. Thus, one would expect some degree of cancellation between Artic and Antarctic sea ice variability and the associated global mean flux is likely to amount to less than a few percent of the observed TOA annual cycle.

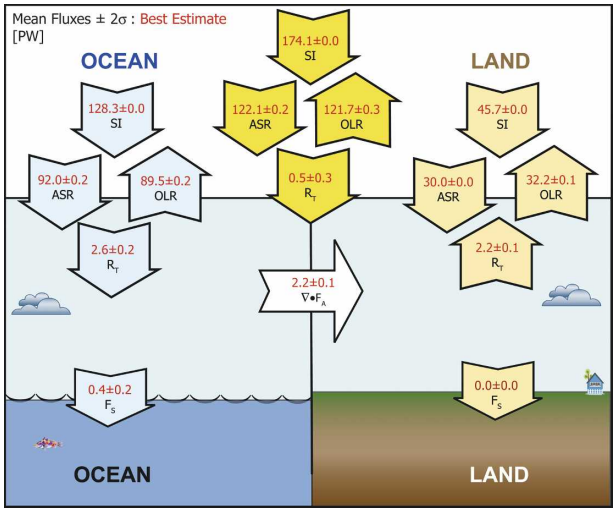

FIG. 2. CERES-period-mean best-estimate FM1 TOA fluxes (PW) globally and for the (right) global land and (left) global ocean regions.

g. Regridding and standard deviations

To provide a consistent delineation of land–sea boundaries among the various datasets described above, all fields are transformed to a grid containing 192 evenly spaced longitudinal grid points and 96 Gaussian-spaced latitudinal grid points using bilinear interpolation (i.e., to a T63 grid; 1.875° latitude). Spatial integrals are calculated using Gaussian weights over the T63 grid and a common land–sea mask is applied. Monthly mean values are used for all calculations. In quantifying the annual cycle variability, the estimated population standard deviation S of the monthly mean values is used and so it relates to the amplitude of the seasonality.

3. Mean fluxes for ERBE and CERES periods

Figure 2 summarizes the best-estimate CERES period (March 2000–May 2004) mean fluxes and $2\sigma_I$ for the global, global land, and global ocean domains. The corresponding global mean terms for the TOASRB, CERES ERBE-like, ERBE-tuned, and ERBE-raw fields are summarized in Table 2. For SI, the same total solar irradiance (1365 W m^{-2}) is used for all estimates with negligible $2\sigma_I$, corresponding to solar insolation of 174.1 ± 0.0 PW globally (but note the systematic uncertainty in Table 1). The TOA SI flux in all estimates is partitioned into 45.7 ± 0.0 PW for land and

TABLE 2. Global mean TOA fluxes and attributes from a variety of sources. Uncertainty ranges represent the $2\sigma_I$ interval.

Source	R_T (PW)	ASR (PW)	OLR (PW)	Albedo
Best estimate, this paper (Mar 2000–May 2004)	0.5 ± 0.3	121.1 ± 0.2	121.7 ± 0.4	0.298 ± 0.001
CERES TOASRB (Mar 2000–May 2004)	3.5 ± 0.3	124.3 ± 0.2	120.9 ± 0.4	0.286 ± 0.001
CERES ERBE like (Mar 2000–May 2004)	2.1 ± 0.3	123.9 ± 0.6	121.8 ± 0.3	0.288 ± 0.003
ERBE tuned (Feb 1985–Apr 1989)	0.0 ± 0.4	119.5 ± 0.1	119.5 ± 0.5	0.313 ± 0.001
ERBE raw (Feb 1985–Apr 1989)	4.6 ± 0.6	123.7 ± 1.3	119.0 ± 1.5	0.293 ± 0.004

128.3 ± 0.0 PW for ocean. The best estimate of the global mean ASR is 122.1 ± 0.2 PW and corresponds to a global mean albedo of 0.298 ± 0.001. The global ocean ASR is 92.0 ± 0.2 PW and the global land ASR is 30.0 ± 0.0 PW. A global mean best-estimate OLR flux of 121.7 ± 0.3 PW largely balances ASR, resulting in R_T = 0.5 ± 0.3 PW. Over ocean, R_T (2.6 ± 0.2 PW) is substantially greater than the global value, and the albedo (0.283 ± 0.002) is substantially lower than for the global mean. An associated imbalance exists between ASR and OLR (89.5 ± 0.2 PW). Conversely, over land, the OLR of 32.2 ± 0.1 PW exceeds ASR, and the albedo is higher (0.346 ± 0.001) than for the global mean.

A net divergence of energy (Table 3) from ocean to land of 2.2 ± 0.1 PW is implied from the combination of the best-estimate TOA budget, the assumption of small annual tendencies in the atmosphere, and the established negligible mean flux and variability in F_S over land (Huang 2006). If divergence is calculated explicitly from the reanalyses during the ERBE period, the NRA and ERA-40 estimates of the ocean to land flux are 2.3 ± 0.2 PW and 1.8 ± 0.8 PW, respectively (see Fig. 8, presented and discussed later). For the CERES period, during which time the ERA-40 fields are not available, an increased divergence of 2.7 ± 0.2 PW in NRA is found (see Fig. 8). The F_S^o (Fig. 2) is based on values from Willis et al. (2004) for 1996–2003. Values from 2003 through 2005 contain considerable uncertainties that are likely associated with inhomogeneities in the observational record, as data from new Argo floats have become available, so that the in situ record is incompatible with satellite altimetry (Lombard et al. 2006). Explicit calculation of $\delta A_E/\delta t$ (Table 3) supports the assumption of a negligible contribution from $\delta A_E/\delta t$; as during the ERBE period, the mean atmospheric tendencies reported by NRA and ERA-40 are 0.0 ± 0.1 PW and 0.0 ± 0.0 PW, respectively. During the CERES period, NRA reports a tendency of 0.0 ± 0.1 PW. Thus, the differences between the estimates of the ocean to land transport are likely associated with errors in the TOA fluxes projected onto the land–ocean residual calculation, and errors in the reanalysis fields. From comparison of ERA-40 and NRA during the ERBE period, the latter are on the order of 0.5 PW.

TABLE 3. Net atmospheric global ocean total energy divergences and tendencies for the ERBE (February 1985–April 1989) and CERES (March 2000–May 2004) periods. Uncertainty ranges represent $\pm 2\sigma_I$ intervals.

	$\nabla \cdot \mathbf{F}_A$	$\delta A_E/\delta t$ (ocean)	$\delta A_E/\delta t$ (land)
NRA (Feb 1985–Apr 1989)	2.3 ± 0.2	0.0 ± 0.2	0.0 ± 0.1
ERA (Feb 1985–Apr 1989)	1.8 ± 0.8	0.0 ± 0.1	0.0 ± 0.0
NRA (Mar 2000–May 2004)	2.7 ± 0.2	0.0 ± 0.1	0.0 ± 0.1

4. The global mean annual cycle

For the annual cycle at the TOA, Fig. 3 shows the global mean, global ocean, and global land R_T and albedo for the ERBE-tuned and CERES best-estimate FM1 and FM2 fields, with $\pm 2\sigma_I$ also shown (shading). The characteristics of the global, global ocean, and global land annual cycles, including uncertainty estimates, are summarized in Tables 4, 5, and 6, respectively. The annual mean has been removed from these values. As differences in seasonal characteristics among the data sources are small, only best-estimate characteristics are reported and only the ERBE-tuned and best-estimate fields are plotted.

Globally, the R_T variations are characterized by an annual maximum in February of 4.3 PW, somewhat after the perihelion, because of the albedo changes from January to February. Then, there is a rapid decline during boreal spring to a minimum of −5.2 PW in June, followed by an increase from June through the following February. Fluctuations in albedo exhibit a significant semiannual cycle with maxima occurring in May and November. Over the global ocean, whose areal extent is biased significantly toward the Southern Hemisphere, R_T peaks at 8.0 PW during austral summer and achieves a minimum of −9.7 PW during austral winter. Uncertainty in the annual cycle of R_T over ocean is nonnegligible. Over land, which is disproportionately located in the Northern Hemisphere, R_T peaks at 4.5

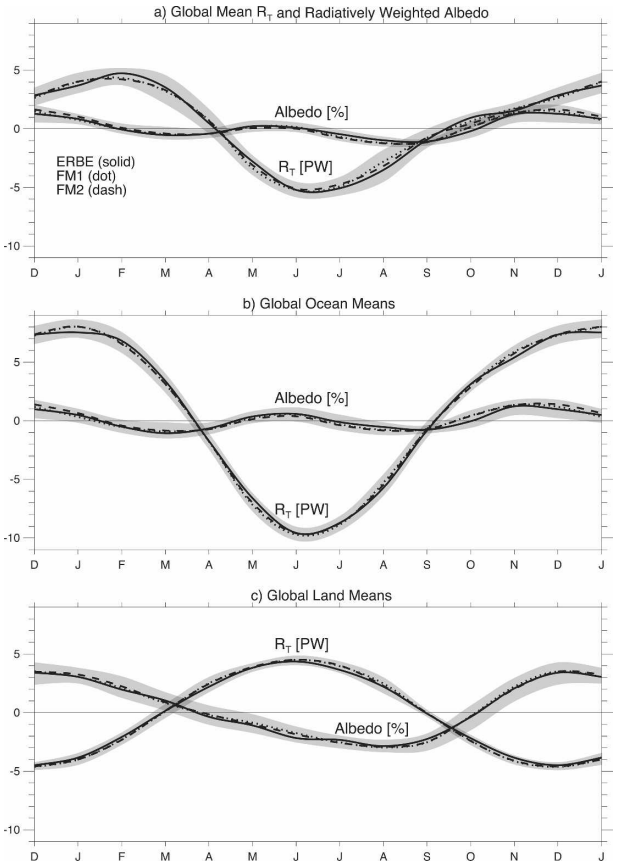

FIG. 3. (a) Global, (b) global ocean, and (c) global land mean annual cycles of albedo (%) and R_T (PW) where shading represents $\pm 2\sigma_I$ of the monthly means and the annual mean has been removed.

PW in June and reaches a minimum of −4.6 PW in December.

Globally, the R_T maximum (Fig. 3) in February is comprises an ASR maximum of 3.1 PW (Fig. 4) and an OLR minimum of −1.6 PW. Peak OLR of 2.2 PW occurs in August with the minimum in ASR of −3.8 PW in June, but the OLR changes correspond mostly to the land contribution, and coincide with the phase of the surface temperature in the Northern Hemisphere. Uncertainty in ASR, particularly for Δ_D, is substantially greater than for OLR. For the global ocean (Fig. 4b), the seasonal cycle is dictated largely by ASR, which reaches a maximum of 7.6 PW in January and a minimum of −9.5 PW in June. The annual cycle of OLR over the global ocean is small, with a −0.6 PW minimum in May and 0.7-PW peak in August. Over land, peak ASR of 5.7 PW occurs in June with a minimum of −5.6 PW in December. The range of uncertainty associated with $\pm 2\sigma_I$ for R_T, ASR, and OLR (shading in Fig. 4) is larger than the differences between the ERBE-tuned and best-estimate FM1 and FM2 fields for all months. Thus, the possibility that differences between the ERBE and CERES estimates result from the different time periods considered cannot be ruled out.

The seasonal cycle of $\delta A_E/\delta t$ is nonnegligible (Fig. 5), increasing during boreal spring and decreasing during late boreal summer and early autumn with a peak in $\delta A_E/\delta t$ of 1.3 PW in June and a minimum of −1.8 PW in September. Over ocean, the relatively small annual cycle of $\delta A_E/\delta t$ peaks in boreal summer and winter near 0.5 PW and reaches a minimum of −0.8 PW in September. The atmospheric total energy divergent flux $\nabla \cdot \mathbf{F}_A$ over ocean (Fig. 5) peaks at 5.2 PW during boreal winter and achieves a minimum during summer of −1.1 PW. The mean ocean–land flux is thus dictated largely by exchanges during boreal winter. Over land the annual cycle of $\delta A_E/\delta t$ is greater than that over ocean and $\nabla \cdot \mathbf{F}_A$, by constraint, balances that over ocean.

The annual cycle of F_S from (2) resembles that of R_T (with opposite sign) (cf. Fig. 6 and Fig. 3), with an F_S maximum of 6.3 PW occurring in austral winter and a minimum of −4.0 PW occurring in austral summer, based on CERES–NRA estimates over ocean and CLM-modeled fields over land, as compared with 5.3 PW and −4.2 PW for R_T. The global ocean annual cycle (Fig. 6), with a maximum of 7.1 PW and minimum of −4.5 PW, is approximately in phase with the global annual cycle. Estimates of F_S^o based on the residual methods of (2) (solid line), which relies primarily on R_T and $\nabla \cdot \mathbf{F}_A$, and (5), which relies on R_T and F_S^l from the CLM, agree closely through the annual cycle, providing an initial estimate of the uncertainty associated with $\nabla \cdot \mathbf{F}_A$ and the assumptions in (2) discussed in section 2. The difference between the methods is less than, or comparable to, the uncertainty associated with $\pm 2\sigma_I$ (shading) for all months, and the main differences occur in northern winter and may reflect uncertainties in land snow and ice (Qian et al. 2006). Here, F_S^l (Fig. 6)

TABLE 4. Characteristics of the best-estimate global mean annual cycle standard deviation S (PW). Uncertainty estimates ($2\sigma_I$ and Δ_{DI}) are provided where possible.

Characteristic	R_T	ASR	OLR	SI	Albedo
$S \pm 2\sigma_I$	3.4 ± 0.1	2.1 ± 0.1	1.5 ± 0.1	4.2 ± 0.0	0.010 ± 0.001
Δ_D	0.3	0.5	0.0	0.0	0.003

TABLE 5. Characteristics of the global ocean mean and annual cycle standard deviation S (PW). Uncertainty estimates ($2\sigma_I$ and Δ_D) are provided where possible.

Characteristic	R_T	ASR	OLR	SI	Albedo
Mean $\pm 2\sigma_I$	2.6 ± 0.2	92.0 ± 0.2	89.5 ± 0.2	128.3 ± 0.0	0.283 ± 0.002
$S \pm 2\sigma_I(S)$	6.4 ± 1	6.2 ± 0.2	0.4 ± 0.1	9.3 ± 0.0	0.009 ± 0.001
Δ_D	0.4	0.5	0.0	0.0	0.004

is out of phase by approximately 5 months, with a maximum of 0.9 PW occurring in November and a minimum of −1.0 PW during May. Interannual variability is dominated by variability over ocean on the order of 0.3 PW as the CLM fields suggest negligible interannual variability over land (<0.1 PW).

A comparison between inferred and direct estimates of O_E during the ERBE period (Fig. 7), along with their rates of change, reveals that the seasonal peak in O_E follows the austral summer, when the global mean peaks in SI and R_T occur, and when the Southern Hemisphere experiences substantial net TOA and surface heating. The magnitude of the March–April peak in O_E varies considerably among the datasets, with estimates from F_S based on ERBE + ERA (not shown) and ERBE + NRA at 3.0×10^{22} J, GODAS at 3.2×10^{22} J, *WOA* at 4.2×10^{22} J, and JMA at 4.5×10^{22} J. During austral winter, O_E falls sharply, reaching estimated minima for F_S (both ERBE–ERA and ERBE–NRA) of -2.8×10^{22} J, for GODAS of -3.6×10^{22} J, for *WOA* of -3.91×10^{22} J, and for JMA of -4.01×10^{22} J. The ocean temperature datasets thus imply a substantially larger annual cycle of O_E than do the F_S estimates, with the annual cycle standard deviation S of $\delta O_E/\delta t$ being greater than inferred from F_S ($S = 5.9$ PW for *WOA*, 5.1 ± 1.7 PW for GODAS, 6.1 ± 2.0 PW for JMA, and 4.4 ± 1.0 PW for ERBE–NRA F_S, where uncertainty estimates represent $2\sigma_I$).

5. Discussion

The estimates presented herein build upon the wide array of estimates currently available and reviewed by Kiehl and Trenberth (1997). Improvements have been made possible by both the newly available CERES fields, and recent considerations of the net planetary imbalances from global ocean and global land energy tendencies. At the TOA, the estimated sampling error ($\pm 2\sigma_I$) associated with the interannual variability of the global annual mean agrees well with the early estimates (Ardanuy et al. 1992; Kyle et al. 1993). For many terms the sampling error is considerably smaller than the differences among the data at different times (Table 2) and hence the importance of errors in the retrieval process is highlighted as a fundamental limitation on our current estimates. The best-estimate values of ASR (albedo) reported here lie above (below) the ERBE-tuned estimates and below (above) the TOASRB, ERBE-raw, and CERES ERBE-like estimates. Confidence in the best-estimate exceeds that in the raw retrievals as the ASR − OLR differences in the untuned products are substantially greater than are allowed for by the existing planetary imbalances. The best-estimate albedo lies toward the lower end of the range of earlier estimates (presented by Kiehl and Trenberth 1997). The global OLR value in Fig. 2 corresponds to 239 W m^{-2}, which is larger than the 235 W m^{-2} estimated by Kiehl and Trenberth (1997) based on ERBE data without the adjustments in appendix B. The ASR of the ERBE-raw and CERES ERBE-like estimates contain significantly greater uncertainty because of interannual variability ($2\sigma_I$) than do the CERES product or the tuned ERBE product, suggesting that the ERBE-retrieval methods or discontinuities associated with the loss of *NOAA-9* (Trenberth 1997) may artificially inflate σ_I. Other aspects of the TOA budget are obscured primarily by the limited span of the observational record. The significance of the differences in monthly deviations from the annual mean is an example of such a quantity, as for all terms, the ERBE-tuned and CERES best-estimate differences are less than $2\sigma_I$ (Figs. 3–5).

TABLE 6. Characteristics of the global land mean and annual cycle standard deviation S. Uncertainty estimates ($2\sigma_I$ and Δ_D) are provided where possible.

Characteristic	R_T (PW)	ASR (PW)	OLR (PW)	SI (PW)	Albedo
Mean $\pm 2\sigma_I$	−2.2 ± 0.4	30.0 ± 0.0	32.2 ± 0.1	45.7 ± 0.0	0.346 ± 0.001
$S \pm 2\sigma_I(S)$	3.5 ± 0.1	4.5 ± 0.1	1.2 ± 0.1	5.3 ± 0.0	0.025 ± 0.002
Δ_D	0.0	0.0	0.0	0.0	0.000

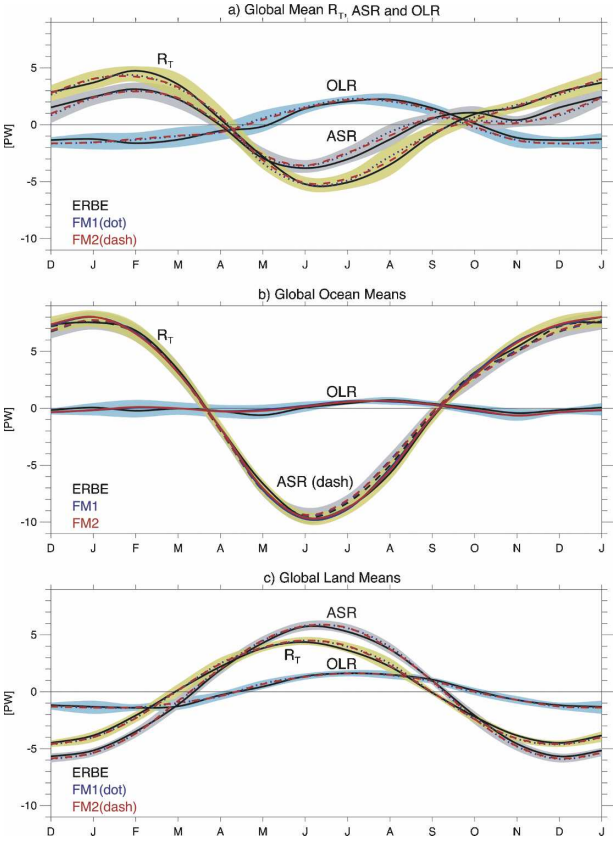

FIG. 4. (a) Global, (b) global ocean, and (c) global land mean annual cycles for ASR, OLR, and R_T (PW), where shading represents $\pm 2\sigma_I$ of the monthly means and the annual mean has been removed.

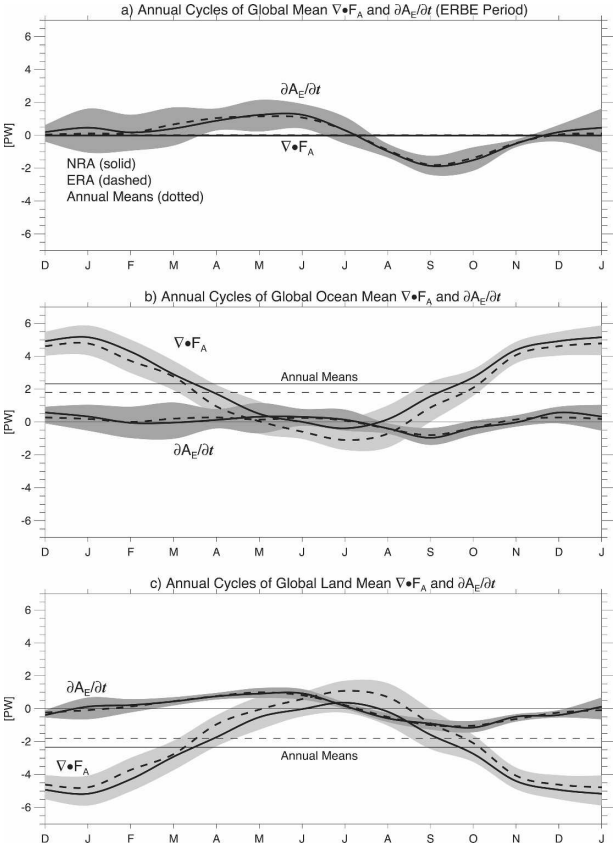

FIG. 5. (a) Global, (b) global ocean, and (c) global land estimates of the atmospheric total energy divergence ($\nabla \cdot \mathbf{F}_A$) and tendency ($\delta A_E/\delta t$; PW) are shown where shading represents $\pm 2\sigma_I$ of the monthly means and the annual mean is shown (dotted).

Within the atmosphere the NRA depict a mean ocean to land transport of near 2 PW during the ERBE period (Fig. 8), consistent with inferences from the TOA fluxes (Fig. 2). However, during the CERES period, the computed NRA land–ocean transport is 2.7 ± 0.2 PW (Table 3), a value that is inconsistent with R_T^I. The ERA-40 estimates are less consistent over time than are those of NRA and the inconsistencies are associated, in part, with established shortcomings of the ERA-40 fields during the 1990s (Uppala et al. 2005). In particular, major changes in the observing system occurred with the introduction of SSM/I data in 1987 (which were not used in NRA) and problems occurred following the Mount Pinatubo eruption in 1991, whose aerosol contaminated the radiances that were assimilated in ERA-40 (whereas NRA used retrievals) (Uppala et al. 2005). Other changes in Fig. 8 affected both reanalyses, albeit differently—in particular, the change from Television and Infrared Observation Satellite (TIROS-N) Operational Vertical Sounder (TOVS) to the Advanced TOVS (ATOVS) in NRA from 1998 to 2001. Accordingly, the decadal variability in Fig. 8 is largely spurious and certainly is not reproducible.

However, the variabilities in the ocean-to-land energy transport from NRA and ERA-40 over time (Fig. 8) are among the most temporally extensive estimates of the atmospheric energy budget. They are compared (Fig. 8) with the transport as inferred from the ERBE-tuned and CERES best-estimate fluxes per (3) using NRA estimates of $\delta A_E/\delta t$. Large interannual variability is mostly real and corresponds to ENSO in part, and includes the sharp increases in 1992–94 and 1997–98, which coincide with El Niño events, and the subsequent declines in 1999–2000, which accompany a transition to La Niña conditions (Trenberth et al. 2002). Lower-frequency variability, including the increase in transport from the mid-1980s through the mid-1990s, is also notable but cannot be confirmed owing to the observing system changes, although these are smaller for NRA.

While the reanalyses are susceptible to changes in their input data, early satellite platforms including

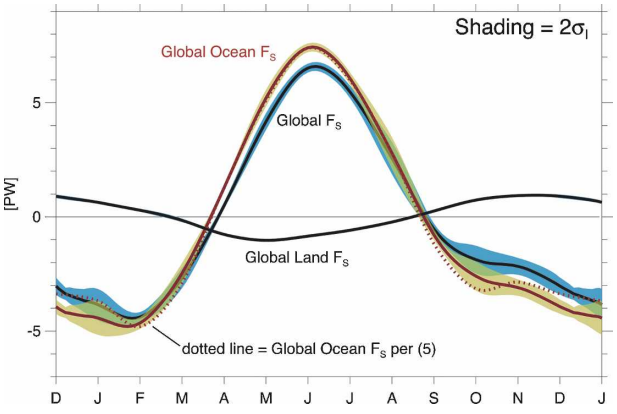

FIG. 6. Global, global ocean, and global land estimates of the net upward surface flux (F_S; PW) are shown where shading represents $\pm 2\sigma_I$ of the monthly means. Global ocean estimates are derived from (2) except for the dotted line, which is derived from (5).

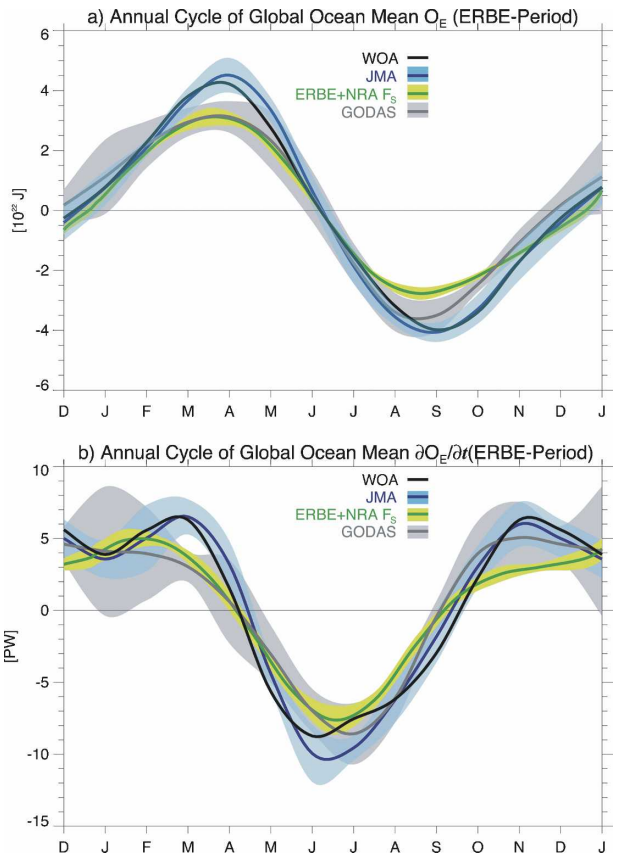

FIG. 7. Annual cycles of (a) O_E ($\times 10^{22}$ J) and (b) $\delta O_E/\delta t$ (PW) are shown with ranges of uncertainty $\pm 2\sigma_I$ for the monthly means from the GODAS and JMA datasets (shading). The GODAS fields have been extended in latitude using the JMA fields, O_E estimates were differenced to provide $\delta O_E/\delta t$, and F_S was integrated in time to provide the O_E anomalies for the ERBE and NRA data.

Nimbus-7, the ERBE, and *ERBS* (Kyle et al. 1993) contain significant uncertainty because of their limited sampling rate and spatial coverage, and their reliance on recalibration methods following major outages and gradual calibration drifts associated with sensor and orbital degradation over time (Trenberth 2002). While the ERBE and CERES retrievals capture aspects of the NRA transport, including the magnitude of the transport during the ERBE period and the decline in transport early in the ERBE period, other significant differences exist, especially including the magnitude and variability of the transport during the CERES period. For these reasons, among others, it is thus not possible to distill the differences in decadal variability from NRA, ERBE, and CERES estimates into their real and spurious components, as natural variability is likely to be large. The susceptibility of discrete observation periods, such as those of ERBE and CERES (shaded), or estimates based on intermittently observed data, such as the reanalyses, to low-frequency variability is therefore real and needs to be quantified in any attempt to more generally assess the energy budget in the context of climate change. The present analysis shows that current datasets are not able to adequately achieve these standards and long-term variability in the budget remains a substantial and open science question.

Globally, the annual cycle of R_T is influenced primarily by ASR and secondarily, though importantly, by OLR. About 80% of the seasonality in SI projects onto ASR—more than would be expected from a globally uniform and constant albedo (70%) owing to the interaction of the spatial and temporal variabilities of albedo with SI. The phase of the global mean ASR is determined primarily by the seasonal cycle of SI, which is governed by Earth's orbit. The annual cycle of the global ocean albedo is predominantly semiannual, with peak values leading the solstices slightly, and minima in March and September coincide with the equinoxes and are associated with the cross-equatorial migration of the intertropical convergence zone. The global ocean (Fig. 4b) seasonal cycle of OLR is small relative to that over land, and there is a near cancellation in OLR variability over ocean between the hemispheres. In contrast, over land (Fig. 4c), both ASR and OLR contribute significantly to the annual cycle of R_T, and significant hemispheric asymmetries project onto the global mean. Albedo over land peaks in boreal winter and varies in a manner consistent with the enhancement of surface albedo due to increased winter snow and ice extent. Globally, the seasonal cycle of R_T is balanced primarily by F_S^o and the contribution of $\delta A_E/\delta t$ is secondary (globally $\nabla \cdot \mathbf{F}_A \equiv 0$). For the global ocean do-

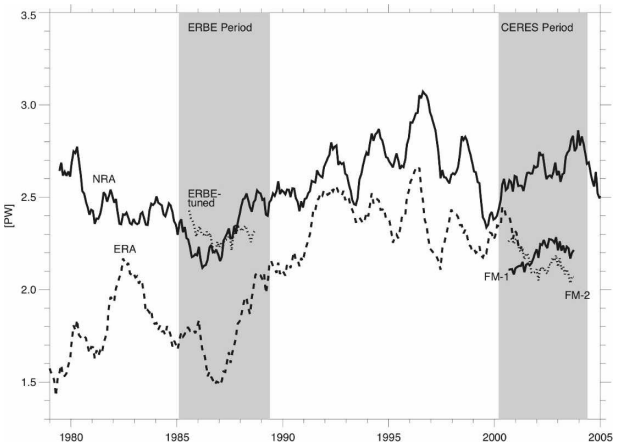

FIG. 8. Interannual variability in the inferred net ocean-to-land energy transport (PW) is shown by 12-month running means for the ERBE and CERES best-estimate R_T over land and NRA $\delta A_E/\delta t$ fields. Transports calculated directly from the NRA and ERA-40 fields are also shown.

main, therefore, a near balance occurs between the TOA radiation and surface fluxes but also with important seasonal contributions from the transport of energy from ocean to land in northern winter, and vice versa in southern winter (albeit much weaker). These aspects are seen more clearly in Fasullo and Trenberth (2008), who report on the meridional structure of these changes.

The annual cycle of the O_E estimates from *WOA* and JMA significantly exceed (~30%) that which can be accounted for by both the TOA and surface energy budgets. Indeed, the differences between the ocean temperature datasets are themselves quite large and agreement between the F_S and GODAS fluxes is better than for *WOA* and JMA. More detailed regional investigations of the spatial structure of the differences in O_E (Fasullo and Trenberth 2008) reveal that the biggest problems lie over the southern oceans, where the scarcity of observations suggests shortcomings in the ocean datasets.

Although changes in R_T have been reasonably matched to changes in O_E (Hansen et al. 2005; Willis et al. 2004), systematic errors remain to be addressed. However, the mean fields and the links between TOA, atmospheric, and surface fluxes, particularly with regard to $\nabla \cdot \mathbf{F}_A$ and O_E, are found to be insufficient for climate change purposes, as the uncertainties are too large. The likely uncertainties in O_E, especially in the Southern Hemisphere (Fasullo and Trenberth 2008), can alter apparent trends if the ocean observing system changes, as it has in recent years with Argo floats (Gouretski and Koltermann 2007), and may be a source of the discrepancy between the O_E tendencies and sea level changes (Lombard et al. 2007); a topic addressed more completely in Trenberth and Fasullo (2008). An additional and significant challenge in understanding the relationship between the energy budget and climate change is posed by the large temporal gaps in the observational record, which render natural variability indistinguishable from calibration drift and error, and platform-related hardware differences.

6. Concluding remarks

The budget established herein (Fig. 2) is thought to improve substantially upon previous estimates [summarized in Kiehl and Trenberth (1997) and Wunsch (2005)] by including CERES retrievals, by adjusting TOA fluxes to recent estimates of the global land and global ocean imbalances, and by including a consideration of the annual cycle of all terms and an assessment of errors. Associated best estimates of albedo and ocean to land fluxes are also derived. The annual cycle of R_T is found to be substantial and is augmented by variability in albedo and OLR. CLM estimates of F_S^l show it to be both an important contributor to the annual cycle of F_S globally and associated with a strong seasonal cycle in $\nabla \cdot \mathbf{F}_A$ over land. The annual mean net flow from ocean to land is on the order of 2% of the total incoming and outgoing radiation (122 PW or globally 239 W m^{-2}) and 4.4 times the estimated net imbalance associated with global warming. Accordingly, it is important for models to be able to capture the land and ocean albedo and, thus, snow cover, vegetation, and cloud cover characteristics, which all vary considerably on a monthly basis. The annual cycle of the net radiation has a range of 9.5 PW and thus is about 8% of the net flow through the system. Hence, a 5% error in the annual cycle is comparable to the climate change signal. Although the global net radiation is dominated by orbital effects, changes in planetary albedo are nontrivial and OLR contributes significantly to enhancing the amplitude of the annual cycle.

The differences in the land and ocean energy budgets are considerable. There is an annual cycle in land energy storage on the order of 2 PW, associated with flows of moisture onto land and the return river flows plus the changes in water storage in both liquid and solid forms. However, the small variability of L_E contrasts with that of O_E, which has a range of 11.6 PW (for F_s; Fig. 6) or nearly 10% of the net flow through the system. Accordingly, over 5 PW of energy flows from ocean to land in northern winter (Fasullo and Trenberth 2008).

The present study also identifies some key uncertainties that limit our present understanding of the budgets

and the earth's climate balance. Variability in F_S across the annual cycle is shown to be at odds with the observations of O_E, a difference that is attributed largely to errors in the ocean analyses. In addition, variability over time, as indicated by σ_I, is substantial for some terms, so that sampling issues are significant contributors to the overall uncertainty. On the interannual time scale, uncertainties are significant for all aspects of the budget and relate to the challenges posed by episodic observations of the budget, in the context of platform calibration issues and hardware inconsistencies, intertwined with significant natural variations. Specifically, reanalyses are shown to be unable to resolve $\nabla \cdot \mathbf{F}_A$ to the accuracy required to diagnose global ocean F_S from TOA imbalances in a changing climate. Progress on the TOA issues is assured through ongoing work in the CERES project (Wong et al. 2006; Wielicki et al. 2006). In the interim, we have made plausible assumptions in adjusting these to provide new estimates of the global radiation budget and its annual cycle. In the atmosphere, reanalyses exhibit inconsistencies related to differences in the data assimilated and the data changes over time, and the need for improvements have been identified. The uncertainties are explored in more detail as we examine the meridional structure or energy storage and flows (Fasullo and Trenberth 2008) and a more in-depth analysis of the ocean (Trenberth and Fasullo 2008). Further refinements in these key uncertainties are likely to contribute substantially to a more complete understanding of the flow of energy through the climate system and its role in our changing climate.

Acknowledgments. This research is partially sponsored by the NOAA CLIVAR and CCDD programs under Grant NA07OAR4310051. CERES data were obtained from the NASA Langley Distributed Data Archive. We thank Bruce Wielicki and other members of the CERES team for their thoughtful comments and discussions.

APPENDIX A

List of Acronyms and Variables

A_E	Total atmospheric energy
ASR	Absorbed solar radiation
ATOVS	Advanced TOVS
CERES	Clouds and the Earth's Radiant Energy System
CLM	Community Land Model
ECMWF	European Centre for Medium-Range Weather Forecasts
ENSO	El Niño–Southern Oscillation
ERA-15	15-yr ECMWF Re-Analysis
ERA-40	40-yr ECWMF Re-Analysis
ERBE	Earth Radiation Budget Experiment
ERBS	*Earth Radiation Budget Satellite*
$\mathbf{F}_A$	Atmospheric transport of energy
$\mathbf{F}_O$	Oceanic transport of energy
F_S	Net surface energy flux (turbulent + radiative)
FM1–4	CERES twin-instrument Flight Models 1 and 2 on the *Terra* spacecraft and Flight Models 3 and 4 on the *Aqua* satellite
GODAS	Global Ocean Data Assimilation System
JMA	Japan Meteorological Agency
L_E	Total land energy storage
MODIS	Moderate Resolution Imaging Spectroradiometer
MOM3	Modular Ocean Model, version 3
NCAR	National Center for Atmospheric Research
NCEP	National Centers for Environmental Prediction
NOAA	National Oceanic and Atmospheric Administration
NRA	NCEP–NCAR reanalysis
O_E	Total ocean energy storage
OLR	Outgoing longwave radiation
$P - E$	Precipitation minus evaporation
PW	Petawatt
R_T	Net TOA radiation
SI	Solar irradiance
SSM/I	Special Sensor Microwave Imager
TIROS	Television and Infrared Observation Satellite
TOA	Top of the atmosphere
TOASRB	TOA surface radiation budget
TOVS	TIROS Operational Vertical Sounder
TSI	Total solar irradiance
T42	Triangular truncation at wavenumber 42 (about 2.8° grid)
WOA	*World Ocean Atlas*

APPENDIX B

Method for Adjusting ERBE-Adjusted Fluxes

ERBE estimates are based on observations from three satellites (*ERBS*, *NOAA-9*, and *NOAA-10*) using both scanning and nonscanning radiometers. Data from ERBE are reported on a 2.5° grid and span from February 1985 to December 1989. While the *NOAA-9* and *-10* satellites were sun-synchronous and polar orbiting, thus providing diurnally biased observations, *ERBS* was in a slowly precessing 57° inclined orbit that allowed for complete diurnal sampling in a 72-day period and thereby helped reduce the impact of diurnal alias-

ing during the ERBE period. Trenberth (1997) provides a detailed discussion of the errors and processing of the original ERBE data (hereafter referred to as ERBE raw), including adjustments to the ERBE data to ensure some homogeneity across the mission when *NOAA-9* was lost and the observations were reduced to those from three to two satellites. In addition, a subsequent adjustment was to the albedo to enforce a global energy balance of zero, consistent with the changes in O_E for this period (Levitus et al. 2005) (referred to as ERBE tuned).

During the course of our investigation it was discovered that the global corrections made in Trenberth (1997) should have discriminated between land and ocean, as analysis of those domains separately clearly revealed a discontinuity when *NOAA-9* failed. Additional steps were therefore taken to remove this error. The failure of the afternoon-orbiting *NOAA-9* satellite was found to be associated with a spurious reduction in retrieved OLR over land, where the diurnal cycle is large and maximum OLR occurs during afternoon. Accordingly, an OLR increase over land following the *NOAA-9* failure of 2.95 W m^{-2} is imposed. Along with compensating for diurnal aliasing, this correction has the beneficial effect of yielding continuity in the inferred ocean to land transport. The difference in global mean OLR prior to and following the failure of *NOAA-9* (+0.37 PW) closely matches the difference reported by the temporally continuous *ERBS* retrievals (+0.39 PW), further justifying this approach.

The original data at T63 resolution from Trenberth (1997) are available online (http://www.cgd.ucar.edu/cas/catalog/satellite/erbe/means2.html). The steps taken include the following:

1) Adjust OLR—An increase to OLR over land is prescribed to match the spurious discontinuity of +2.95 W m^{-2}. OLR over ocean is not altered. It is then found that the associated ocean to land flux is approximately continuous through the *NOAA-9* transition. Also, the difference between the post- and pre-*NOAA-9* failure global mean OLR values (+0.39 PW) is found to agree approximately with the 60°S–60°N difference from *ERBS* [+0.37 PW; Wong et al. (2006)].
2) Retune reflected and absorbed solar radiation—The adjustment is required to reset the $R_T = 0$ as per Levitus et al. (2005). Absorbed and reflected solar radiations are adjusted in tandem such that they total to the original solar insolation. A tuning parameter, α, is derived empirically to satisfy this criterion. If f is the ratio of the new global bias to the global mean ASR, then a new ASR is derived from $\mathrm{ASR}_{\mathrm{net}} = \mathrm{ASR}(1 - f)/\alpha$, which is solved empirically to give $\alpha = 1.0055$. The ASR scaling contributes to a few instances where ASR < 0 and thus ASR is reset to 0.

REFERENCES

Antonov, J. L., S. Levitus, and T. P. Boyer, 2004: Climatological annual cycle of ocean heat content. *Geophys. Res. Lett.,* **31,** L04304, doi:10.1029/2003GL018851.

Ardanuy, P. E., H. L. Kyle, and D. Hoyt, 1992: Global relationships among the earth's radiation budget, cloudiness, volcanic aerosols, and surface temperature. *J. Climate,* **5,** 1120–1139.

Barkstrom, B. R., and J. B. Hall, 1982: Earth Radiation Budget Experiment (ERBE)—An overview. *J. Energy,* **6,** 141–146.

Behringer, D. W., 2007: The Global Ocean Data Assimilation System (GODAS) at NCEP. Preprints, *11th Symp. on Integrated Observing and Assimilation Systems for the Atmosphere, Ocean, and Land Surface,* San Antonio, TX, Amer. Meteor. Soc., 3.3. [Available online at http.//ams.conf.com/ams/pdfpapers/119541.pdf.]

——, and Y. Xue, 2004: Evaluation of the global ocean data assimilation system at NCEP: The Pacific Ocean. Preprints, *Eighth Symp. on Integrated Observing and Assimilation Systems for Atmosphere, Oceans, and Land Surface,* Seattle, WA, Amer. Meteor. Soc., 2.3. [Available online at http://ams.confex.com/ams/pdfpapers/70720.pdf.]

Bonan, G. B., K. W. Oleson, M. Vertenstein, S. Levis, X. B. Zeng, Y. J. Dai, R. E. Dickinson, and Z. L. Yang, 2002: The land surface climatology of the community land model coupled to the NCAR Community Climate Model. *J. Climate,* **15,** 3123–3149.

Dai, A. G., and K. E. Trenberth, 2002: Estimates of freshwater discharge from continents: Latitudinal and seasonal variations. *J. Hydrometeor.,* **3,** 660–687.

Dines, W. H., 1917: The heat balance of the atmosphere. *Quart. J. Roy. Meteor. Soc.,* **43,** 151–158.

Fasullo, J. T., and K. E. Trenberth, 2008: The annual cycle of the energy budget. Part II: Meridional structures and poleward transport. *J. Climate,* **21,** 2314–2326.

Gleckler, P. J., and B. C. Weare, 1997: Uncertainties in global ocean surface heat flux climatologies derived from ship observations. *J. Climate,* **10,** 2764–2781.

Gouretski, V., and K. P. Koltermann, 2007: How much is the ocean really warming? *Geophys. Res. Lett.,* **34,** L01610, doi:10.1029/2006GL027834.

Hansen, J., and Coauthors, 2005: Earth's energy imbalance: Confirmation and implications. *Science,* **308,** 1431–1435.

Huang, S., 2006: Land warming as part of global warming. *Eos, Trans. Amer. Geophys. Union,* **87,** 477, 780.

Ishii, M., M. Kimoto, K. Sakamoto, and S. I. Iwasaki, 2006: Steric sea level changes estimated from historical ocean subsurface temperature and salinity analyses. *J. Oceanogr.,* **62,** 155–170.

Jayne, S. R., and J. Marotzke, 2001: The dynamics of ocean heat transport variability. *Rev. Geophys.,* **39,** 385–411.

Kalnay, E., and Coauthors, 1996: The NCEP/NCAR 40-Year Reanalysis Project. *Bull. Amer. Meteor. Soc.,* **77,** 437–471.

Kiehl, J. T., and K. E. Trenberth, 1997: Earth's annual global mean energy budget. *Bull. Amer. Meteor. Soc.,* **78,** 197–208.

Kistler, R., and Coauthors, 2001: The NCEP–NCAR 50-Year Reanalysis: Monthly means CD-ROM and documentation. *Bull. Amer. Meteor. Soc.,* **82,** 247–267.

Köberle, C., and R. Gerdes, 2003: Mechanisms determining vari-

ability of Arctic ice conditions and export. *J. Climate,* **16,** 2843–2858.

Kyle, H. L., and Coauthors, 1993: The Nimbus Earth Radiation Budget (ERB) Experiment—1975 to 1992. *Bull. Amer. Meteor. Soc.,* **74,** 815–830.

Levitus, S., and J. Antonov, 1997: *Climatological and Interannual Variability of Temperature, Heat Storage, and Rate of Heat Storage in the World Ocean.* NOAA Atlas NESDIS 16, 6 pp. and 186 figs.

——, ——, and T. Boyer, 2005: Warming of the World Ocean, 1955–2003. *Geophys. Res. Lett.,* **32,** L02604, doi:10.1029/2004GL021592.

Locarnini, R. A., A. V. Mishonov, J. I. Antonov, T. P. Boyer, and H. E. Garcia, 2006: *Temperature.* Vol. 1, *World Ocean Atlas 2005,* NOAA Atlas NESDIS 61, 182 pp.

Loeb, N. G., F. Parol, J. C. Buriez, and C. Vanbauce, 2000: Top-of-atmosphere albedo estimation from angular distribution models using scene identification from satellite cloud property retrievals. *J. Climate,* **13,** 1269–1285.

——, and Coauthors, 2007: Multi-instrument comparison of top-of-atmosphere reflected solar radiation. *J. Climate,* **20,** 575–591.

Lombard, A., D. Garcia, G. Ramillien, A. Cazenave, F. Fetchtner, R. Biancale, and M. Ishii, 2007: Estimation of steric sea level variations from combined GRACE and *Jason-1* data. *Earth Planet. Sci. Lett.,* **254,** 194–202.

Qian, T., A. Dai, K. E. Trenberth, and K. W. Oleson, 2006: Simulation of global land surface conditions from 1948 to 2004. Part I: Forcing data and evaluation. *J. Hydrometeor.,* **7,** 953–975.

Trenberth, K. E., 1997: Using atmospheric budgets as a constraint on surface fluxes. *J. Climate,* **10,** 2796–2809.

——, 2002: Changes in tropical clouds and radiation: Are they real? *Science,* **296,** doi:10.1126/science.296.5576.2095a.

——, and C. J. Guillemot, 1998: Evaluation of the atmospheric moisture and hydrological cycle in the NCEP/NCAR reanalyses. *Climate Dyn.,* **14,** 213–231.

——, and J. M. Caron, 2001: Estimates of meridional atmosphere and ocean heat transports. *J. Climate,* **14,** 3433–3443.

——, and D. P. Stepaniak, 2003a: Covariability of components of poleward atmospheric energy transports on seasonal and interannual timescales. *J. Climate,* **16,** 3690–3704.

——, and ——, 2003b: Seamless poleward atmospheric energy transports and implications for the Hadley circulation. *J. Climate,* **16,** 3705–3721.

——, and ——, 2004: The flow of energy through the Earth's climate system. *Quart. J. Roy. Meteor. Soc.,* **130,** 2677–2701.

——, and J. Fasullo, 2008: An observational estimate of inferred ocean energy divergence. *J. Phys. Oceanogr.,* **38,** 984–999.

——, J. M. Caron, and D. P. Stepaniak, 2001: The atmospheric energy budget and implications for surface fluxes and ocean heat transports. *Climate Dyn.,* **17,** 259–276.

——, D. P. Stepaniak, and J. M. Caron, 2002: Accuracy of atmospheric energy budgets from analyses. *J. Climate,* **15,** 3343–3360.

——, J. Fasullo, and L. Smith, 2005: Trends and variability in column-integrated water vapor. *Climate Dyn.,* **24,** 741–758.

——, L. Smith, T. Qian, A. Dai, and J. Fasullo, 2007: Estimates of the global water budget and its annual cycle using observational and model data. *J. Hydrometeor.,* **8,** 758–769.

Uppala, S. M., and Coauthors, 2005: The ERA-40 reanalysis. *Quart. J. Roy. Meteor. Soc.,* **131,** 2961–3012.

Wielicki, B. A., B. R. Barkstrom, E. F. Harrison, R. B. Lee, G. L. Smith, and J. E. Cooper, 1996: Clouds and the Earth's Radiant Energy System (CERES): An Earth Observing System experiment. *Bull. Amer. Meteor. Soc.,* **77,** 853–868.

——, K. Priestley, P. Minnis, N. Loeb, D. Kratz, T. Charlock, D. Doelling, and D. Young, 2006: CERES radiation budget accuracy overview. Preprints, *12th Conf. on Atmospheric Radiation,* Madison, WI, Amer. Meteor. Soc., 9.1. [Available online at http://ams.confex.com/ams/Madison2006/techprogram/paper_112371.htm.]

Willis, J., D. Roemmich, and B. Cornuelle, 2004: Interannual variability in upper-ocean heat content, temperature and thermosteric expansion on global scales. *J. Geophys. Res.,* **109,** C12036, doi:10.1029/2003JC002260c.

Wong, T., B. A. Wielicki, R. B. Lee III, G. L. Smith, K. A. Bush, and J. K. Willis, 2006: Reexamination of the observed decadal variability of Earth Radiation Budget using altitude-corrected ERBE/ERBS nonscanner WFOV data. *J. Climate,* **19,** 4028–4040.

Wunsch, C., 2005: The total meridional heat flux and its oceanic and atmospheric partition. *J. Climate,* **18,** 4374–4380.

Ye, Q., and J. A. Coakley, 1996: Biases in Earth radiation budget observations. 2. Consistent scene identification and anisotropic factors. *J. Geophys. Res.,* **101** (D16), 21 253–21 264.

Yu, R. C., M. H. Zhang, and R. D. Cess, 1999: Analysis of the atmospheric energy budget: A consistency study of available data sets. *J. Geophys. Res.,* **104,** 9655–9661.